International Journal of Engineering and Science Invention (IJESI)
ISSN (Online): 2319-6734, ISSN (Print): 2319-6726
www.ijesi.org ||Volume 15 Issue 1 January 2026 || PP 31-43

Entropy-Aware Design of Arrhenius Reactive Nanofluid Flow over a Moving Wedge

Ramij Raja[1], Dr. Priyanka Bhalerao[2]
[1, 2] *Department of Mathematics, Sri Satya Sai University of Technology & Medical Sciences, Sehore, M.P.*

I. Introduction

This article presents an entropy-aware design framework for an Arrhenius-reactive nanofluid flowing over a moving wedge embedded in a porous medium. The model couples Buongiorno nanoparticle transport (Brownian diffusion and thermophoresis), Rosseland thermal radiation, Darcy resistance, and temperature-sensitive Arrhenius chemistry. Governing equations are reduced by similarity transformation and solved with a Chebyshev spectral-collocation solver augmented by pseudo-arclength continuation to resolve stiff reaction terms and capture ignition/extinction bifurcations. Total entropy production is decomposed into thermal/radiative, viscous/porous, diffusive and chemical-irreversibility contributions and used as an explicit design objective alongside conversion.

Key results show S-shaped multiplicity with well-defined ignition and extinction thresholds; ignited branches have substantially higher temperatures and chemical irreversibility. Entropy budgets shift from thermal/diffusive dominance in extinguished states to chemical and viscous dominance in ignited states. Parametric sweeps reveal that modest changes in nanoparticle transport (Brownian and thermophoretic coefficients) reallocate entropy more effectively than comparable modifications of reaction intensity or wedge geometry. Multi-objective optimization (NSGA-II) produces Pareto fronts with a pronounced knee: knee-region operating points offer the best practical trade-off between conversion and second-law losses. Operating windows identify stable corridors that avoid fold neighborhoods and inform robust design choices.

Conclusions recommend prioritizing nanofluid transport control and Pareto-knee operation, combined with targeted thermal management to expand low-entropy feasible regions. The article notes limitations—Rosseland linearization for moderate ΔT and steady-state stability assessments—and recommends mapping dimensionless groups to experimental systems and performing time-dependent stability studies for practical translation.

Keywords: Arrhenius reactive nanofluid, Entropy generation , Moving wedge flow , Buongiorno model , Thermophoresis and Brownian motion , Ignition–extinction bifurcation , Porous medium , Thermal radiation , multi-objective optimization , Pareto analysis.

II. Literature Review

Because of their better thermal performance than traditional fluids, nanofluids—engineered suspensions of nanoparticles in base fluids—have drawn a lot of attention. Buongiorno [1] provided the theoretical basis for nanofluid transport by showing that thermophoresis and Brownian motion predominate in the movement of nanoparticles within boundary layers. This model became the standard framework for nanofluid flow analysis after resolving inconsistencies in previous single-phase formulations.

By analysing nanofluid boundary-layer flow on a stretching surface using this formulation, Khan and Pop [2] demonstrated how nanoparticle diffusion dramatically changes temperature and concentration fields. Their findings demonstrated that thermophoresis controls the aggregation of nanoparticles close to hot surfaces, but Brownian motion improves heat transfer. These results were expanded to more intricate geometries in later research. In their critical evaluation of nanofluid boundary-layer models, Nield and Kuznetsov [3] stressed that physically valid predictions require the coupling of nanoparticle diffusion with porous media effects.

Additional research focused on curved and sloped surfaces. In their study of nanofluid flow across an inclined stretched cylinder, Eldesoky et al. [12] showed that buoyancy, radiation, and nanoparticle transport all affect the rates of heat and mass transfer. Review studies repeatedly show that nanofluids perform better than conventional fluids in thermal systems at both the micro and macro scales, especially in situations involving high heat flux and restricted geometries [17]. Overall, research shows that a careful balance between surface geometry, convection, and nanoparticle diffusion controls nanofluid boundary-layer behaviour.

Second-law (entropy generation) analysis offers a better understanding of thermodynamic efficiency, whereas first-law analyses assess heat and mass transport. Irreversibility resulting from mass diffusion, temperature gradients, viscous dissipation, and chemical processes are taken into consideration by entropy

generation. One of the first thorough entropy analyses for radiative nanofluid flows was published by Mandal et al. [4], who also showed that thermal radiation greatly increases irreversibility.

Extending entropy analysis to Casson nanofluid flows with Arrhenius activation energy, Ali et al. [5] found that higher activation energy increases entropy formation close to the surface while suppressing heat and mass transmission. Brownian motion and thermophoresis shift entropy sources inside the boundary layer, frequently increasing overall entropy despite greater heat transport, as demonstrated by Parida et al. [9]. In a more recent study, Wu et al. [8] examined entropy generation in radiative nanofluid flows including chemical processes and found that thermal radiation and reaction strength are the main causes of irreversibility.

Additionally, studies that take into account nonlinear radiation effects show that radiative heat transfer significantly boosts entropy creation even though it is advantageous for temperature control [7]. When taken as a whole, these studies show that increases in heat and mass transport do not always translate into thermodynamic optimality, highlighting the significance of entropy-based optimization frameworks.

By adding resistance that modifies temperature and velocity distributions, porous media have a substantial impact on nanofluid movement. In their analysis of heat-transfer enhancement techniques in porous nanofluid systems, Hayat et al. [11] emphasized that Darcy resistance suppresses fluid velocity while thickening thermal boundary layers. Because of decreased convection, it has been demonstrated that porous resistance lowers velocity while raising temperature in wedge and stretched forms.

In their analysis of Eyring–Powell nanofluid flow across a wedge surface, Raju et al. [20] showed that porous drag reduces momentum transmission while increasing thermal boundary-layer thickness. Similar patterns for unsteady Falkner-Skan wedge flows were observed by Ali et al. [18], demonstrating the significant influence of wedge angle and permeability on transport rates.

Effects of magnetic fields have also been thoroughly studied. According to Shah et al. [13], Lorentz forces promote entropy generation through Joule heating while suppressing fluid velocity and improving conductive heat transmission. El Harfouf et al. [19] also showed that thermodynamic irreversibility is increased when non-Fourier heat flow models are coupled with magnetic fields. These findings highlight that whereas magnetic and porous controls are useful for controlling flow, they also result in significant entropy penalties.

Strong nonlinear coupling between temperature and species concentration is introduced by Arrhenius kinetics-driven chemical processes. Higher activation energy lowers reaction rates, causing reactant buildup close to the surface, as demonstrated by Bhatti and Michaelides [14]. According to Ali et al. [5], activation energy has two functions: it increases entropy generation as a result of stronger thermal gradients while suppressing chemical conversion.

In a similar vein, Shah et al. [13] found that higher activation energy increases irreversibility while decreasing heat transmission. On the other hand, activation energy can increase mass transfer while decreasing thermal transport under specific wedge-flow circumstances, according to Ali et al. [18]. These results suggest that rather than being viewed as independent parameters, Arrhenius kinetics should be tuned in tandem with flow geometry and nanoparticle transport.

Although extensive literature exists on nanofluid transport [1–3,12], entropy generation [4,7–9], porous and magnetic effects [11,13,18–20], and Arrhenius reaction kinetics [5,14], their **combined influence in moving wedge configurations remains insufficiently explored**. Most existing studies treat entropy generation as a secondary diagnostic rather than a design objective. Moreover, few investigations explicitly optimize chemical conversion under entropy constraints.

The present work addresses this gap by developing an **entropy-aware Arrhenius-reactive nanofluid model over a moving wedge**, integrating nanoparticle diffusion, porous resistance, and thermal radiation within a unified thermodynamic optimization framework.

III. Mathematical Formulation

Flow Configuration and Coordinate System

Consider the steady, two-dimensional, incompressible boundary layer flow of a chemically reacting nanofluid over a wedge. The wedge is embedded in a fluid-saturated porous medium.The potential flow velocity outside the boundary layer is $U_e(x) = U_0 x^m$. The wedge surface moves with velocity $U_w(x) = \lambda U_e(x)$.Let's assume the following:

- The magnetic field and Joule heating are neglected.
- The fluid is optically thick (Rosseland approximation).
- The Boussinesq approximation is applied solely to the porous drag term; density variations elsewhere are negligible.
- The chemical reaction follows first-order Arrhenius kinetics.

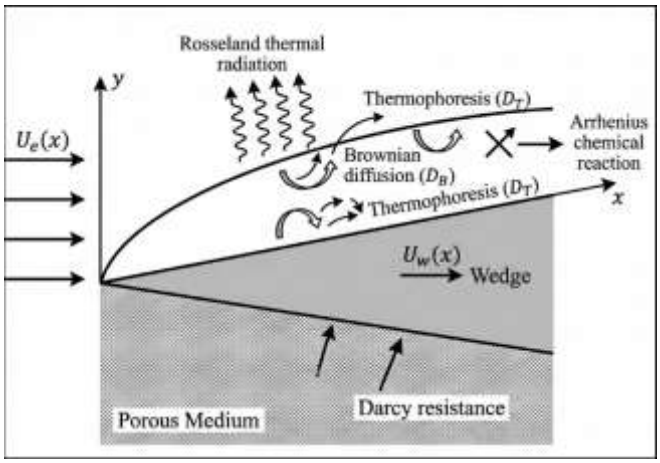

Figure 1. Physical configuration and coordinate system for the Arrhenius-reactive nanofluid flow over a moving wedge.

Governing Conservation Equations

Under the boundary layer approximations ($\partial/\partial x \ll \partial/\partial y$), the governing equations for mass, momentum, energy, and nanoparticle concentration are expressed as follows:

Continuity Equation

$$\frac{\partial u}{\partial x} + \frac{\partial v}{\partial y} = 0 \tag{1}$$

Momentum Equation (Falkner-Skan-Darcy)

This equation balances inertial forces with pressure gradients, viscous diffusion, and porous resistance (Darcy law):

$$u\frac{\partial u}{\partial x} + v\frac{\partial u}{\partial y} = U_e\frac{dU_e}{dx} + \nu\frac{\partial^2 u}{\partial y^2} - \frac{\nu}{K_p^*}(u - U_e) \tag{2}$$

where ν is the kinematic viscosity and K_p^* is the permeability of the porous medium.

Thermal Energy Equation

This equation accounts for convection, radiation, nanoparticle diffusion (Brownian and thermophoretic), and the heat of reaction:

$$u\frac{\partial T}{\partial x} + v\frac{\partial T}{\partial y} = \alpha\frac{\partial^2 T}{\partial y^2} - \frac{1}{(\rho C_p)_f}\frac{\partial q_r}{\partial y} + \tau\left[D_B\frac{\partial C}{\partial y}\frac{\partial T}{\partial y} + \frac{D_T}{T_\infty}\left(\frac{\partial T}{\partial y}\right)^2\right] + \frac{Q}{(\rho C_p)_f}\mathcal{R}_{chem} \tag{3}$$

where:

- $\alpha = k/(\rho C_p)_f$ is the thermal diffusivity.
- $\tau = (\rho C_p)_p/(\rho C_p)_f$ is the ratio of nanoparticle to base fluid heat capacity.
- Q is the heat of reaction coefficient (J/kg).

Radiative Heat Flux (Rosseland Approximation):

$$q_r = -\frac{4\sigma^*}{3k^*}\frac{\partial T^4}{\partial y} \approx -\frac{16\sigma^* T_\infty^3}{3k^*}\frac{\partial T}{\partial y} \tag{4}$$

Substituting this into the energy equation modifies the thermal diffusion term.

Nanoparticle Concentration Equation

This equation governs the transport of nanoparticles due to Brownian motion, thermophoresis, and chemical consumption:

$$u\frac{\partial C}{\partial x} + v\frac{\partial C}{\partial y} = D_B\frac{\partial^2 C}{\partial y^2} + \frac{D_T}{T_\infty}\frac{\partial^2 T}{\partial y^2} - \mathcal{R}_{chem} \tag{5}$$

Arrhenius Reaction Kinetics

The reaction rate $\mathcal{R}_{chem}$ follows Arrhenius temperature dependence:

$$\mathcal{R}_{chem} = k_0 C \exp\left(-\frac{E_a}{R_g T}\right) \tag{6}$$

where k_0 is the pre-exponential factor, E_a is the activation energy, and R_g is the universal gas constant.

Boundary Conditions
The system is subject to the following boundary conditions:

At the wedge surface ($y = 0$):
$$u = U_w(x) = \lambda U_0 x^m, v = 0, T = T_w, C = C_w \quad (7)$$

Far from the surface ($y \to \infty$):
$$u \to U_e(x) = U_0 x^m, T \to T_\infty, C \to C_\infty \quad (8)$$

Similarity Transformations
To transform the PDEs into ODEs, we introduce the following similarity variables:
$$\eta = y\sqrt{\frac{(m+1)U_0}{2\nu x}}, \psi(x,y) = \sqrt{\frac{2\nu U_0 x^{m+1}}{m+1}} f(\eta) \quad (9)$$
from which the velocity components are:
$$u = \frac{\partial \psi}{\partial y} = U_0 x^m f'(\eta), v = -\frac{\partial \psi}{\partial x} = -\sqrt{\frac{\nu U_0 (m+1)}{2x^{m-1}}}\left[f + \frac{m-1}{m+1}\eta f'\right] \quad (10)$$

Dimensionless Temperature and Concentration:
$$\theta(\eta) = \frac{T-T_\infty}{T_w-T_\infty}, \phi(\eta) = \frac{C-C_\infty}{C_w-C_\infty} \quad (11)$$

Non-Dimensional Ordinary Differential Equations
Substituting the transformations into the governing equations yields the following system of nonlinear ODEs:
$$f''' + ff'' + \beta[1-(f')^2] - K_p(f'-1) = 0 \quad (12)$$
$$(1+R_d)\theta'' + Prf\theta' + PrNb\theta'\phi' + PrNt\,(\theta')^2 + PrQ^* Dr\phi \exp\left(\frac{-E}{1+\delta\theta}\right) = 0 \quad (13)$$
$$\phi'' + Lef\phi' + \frac{Nt}{Nb}\theta'' - LeDr\phi\exp\left(\frac{-E}{1+\delta\theta}\right) = 0 \quad (14)$$
$$\eta = 0: f(0) = 0, f'(0) = \lambda, \theta(0) = 1, \phi(0) = 1$$
$$\eta \to \infty: f'(\infty) \to 1, \theta(\infty) \to 0, \phi(\infty) \to 0 \quad (15)$$

The parameters governing the flow physics are defined as:

Parameter	Symbol	Mathematical Definition	Parameter	Symbol	Mathematical Definition
Hartree Pressure Gradient	β	$\frac{2m}{m+1}$	Reaction Damköhler Number	Dr	$\frac{2k_0}{(m+1)U_0 x^{m-1}}$
Porous Drag Parameter	K_p	$\frac{2\nu}{(m+1)U_0 x K_p^*}$	Activation Energy Parameter	E	$\frac{E_a}{R_g T_\infty}$
Prandtl Number	Pr	$\frac{\nu}{\alpha}$	Heat Release Parameter	Q^*	$\frac{Q(C_w-C_\infty)}{(\rho C_p)_f(T_w-T_\infty)}$
Lewis Number	Le	$\frac{\nu}{D_B} = \frac{\alpha}{D_B}Pr$	Temperature Ratio	δ	$\frac{T_w-T_\infty}{T_\infty}$
Radiation Parameter	R_d	$\frac{16\sigma^* T_\infty^3}{3k^* k}$	Velocity Ratio	λ	$\frac{U_w}{U_e}$
Brownian Motion Parameter	Nb	$\frac{\tau D_B (C_w-C_\infty)}{\nu}$	Thermophoresis Parameter	Nt	$\frac{\tau D_T (T_w-T_\infty)}{\nu T_\infty}$

Entropy Generation Analysis

The local volumetric rate of entropy generation (S'''_{gen}) is derived from the second law of thermodynamics and consists of contributions from thermal gradients, viscous dissipation, porous drag, mass diffusion, and chemical reaction:
$$S'''_{gen} = \underbrace{\frac{k+\frac{16\sigma^* T_\infty^3}{3k^*}}{T^2}\left(\frac{\partial T}{\partial y}\right)^2}_{\text{Thermal + Radiative}} + \underbrace{\frac{\mu}{T}\left[\left(\frac{\partial u}{\partial y}\right)^2 + \frac{\nu}{K_p^*}(u-U_e)^2\right]}_{\text{Viscous + Porous}} + \underbrace{\frac{R_g D_B}{C}\left(\frac{\partial C}{\partial y}\right)^2}_{\text{Diffusive}} + \underbrace{\frac{\mathcal{R}_{chem}\,\Delta G}{T}}_{\text{Chemical}} \quad (16)$$
Introducing the characteristic entropy generation scale:

$$S'''_{gen,0} = \frac{k(T_w - T_\infty)^2}{T_\infty^2 L^2}$$

the dimensionless local entropy generation number becomes:

$$N_s(\eta) = \frac{(1+R_d)}{(1+\delta\theta)^2}(\theta')^2 + \frac{Br}{(1+\delta\theta)}\left[(f'')^2 + K_p(f'-1)^2\right] + \frac{\Omega}{(1+\delta\theta)}(\phi')^2 + \frac{\Lambda}{(1+\delta\theta)}Dr\phi\exp\left(\frac{-E}{1+\delta\theta}\right) \quad (17)$$

where: $Br = \frac{\mu U_e^2}{k(T_w - T_\infty)}$ (Brinkman number), $\Omega = \frac{R_g D_B (C_w - C_\infty)^2}{kC_\infty (T_w - T_\infty)}$ (Diffusive irreversibility parameter), $\Lambda = \frac{R_g \mathcal{R}_{chem,0} L^2 \Delta G}{k(T_w - T_\infty)^2}$ (Chemical irreversibility parameter)

The total entropy generation across the boundary layer is:

$$S_{tot} = \int_0^{\eta_\infty} N_s(\eta)\, d\eta$$

The **Bejan number** (Be) quantifies the relative dominance of heat transfer irreversibility compared to the total entropy generation. It is defined as:

$$Be = \frac{N_{s,thermal}}{N_{s,total}}$$

where:

$$N_{s,thermal} = \frac{(1+R_d)}{(1+\delta\theta)^2}(\theta')^2$$

and

$$N_{s,total} = N_{s,thermal} + N_{s,viscous} + N_{s,diffusive} + N_{s,chemical}$$

The **local Bejan number** at position η is:

$$Be(\eta) = \frac{\frac{(1+R_d)}{(1+\delta\theta)^2}(\theta')^2}{N_s(\eta)}$$

The **integral (averaged) Bejan number** is:

$$\overline{Be} = \frac{\int_0^{\eta_\infty} N_{s,thermal}\,(\eta)\, d\eta}{\int_0^{\eta_\infty} N_s(\eta)\, d\eta} = \frac{S_{tot,thermal}}{S_{tot}}$$

Engineering Parameters of Interest

Skin Friction Coefficient

The wall shear stress is: $\tau_w = \mu \frac{\partial u}{\partial y}\Big|_{y=0}$. The local skin friction coefficient is: $C_{f,x} = \frac{\tau_w}{\frac{1}{2}\rho U_e^2} = \frac{2\mu}{\rho U_e^2}\frac{\partial u}{\partial y}\Big|_{y=0}$

In dimensionless form: $C_{f,x}\sqrt{Re_x} = \sqrt{\frac{2(m+1)}{1}} f''(0)$

where $Re_x = U_e x/\nu$ is the local Reynolds number.

Nusselt Number

The wall heat flux is: $q_w = -k_{eff}\frac{\partial T}{\partial y}\Big|_{y=0} = -(k + \frac{16\sigma^* T_\infty^3}{3k^*})\frac{\partial T}{\partial y}\Big|_{y=0}$. The local Nusselt number is: $Nu_x = \frac{q_w x}{k(T_w - T_\infty)}$

In dimensionless form: $\frac{Nu_x}{\sqrt{Re_x}} = -\sqrt{\frac{m+1}{2}}(1+R_d)\,\theta'(0)$

Sherwood Number

The wall mass flux is: $j_w = -D_B\frac{\partial C}{\partial y}\Big|_{y=0}$. The local Sherwood number is: $Sh_x = \frac{j_w x}{D_B(C_w - C_\infty)}$

In dimensionless form: $\frac{Sh_x}{\sqrt{Re_x}} = -\sqrt{\frac{m+1}{2}}\phi'(0)$

Conversion Efficiency

The total chemical conversion within the boundary layer is defined as:

$$\mathcal{C} = \int_0^{\eta_\infty} Dr\phi\exp\left(\frac{-E}{1+\delta\theta}\right) d\eta$$

These integral measures the cumulative reaction extent. It serves as a constraint in the optimization problem where the goal is to achieve a target conversion ($\mathcal{C} \geq \mathcal{C}_{target}$) while minimizing entropy generation.

We define a dimensionless efficiency metric:

$$\eta_{thermo} = \frac{\mathcal{C}}{S_{tot}}$$

This ratio quantifies the chemical productivity per unit of thermodynamic irreversibility. Higher values indicate more efficient operation—achieving greater conversion with lower entropy penalty.

IV. Numerical Methodology

The governing system of coupled, nonlinear boundary value problems (BVPs) in Eqs. (12)–(15) does not admit a closed-form analytical solution due to the stiffness of the Arrhenius source term and the high nonlinearity of the nanofluid transport equations. This section details the **Spectral Collocation Method (SCM)** with **Pseudo-Arclength Continuation** developed to obtain high-precision numerical solutions, as well as the **Multi-Objective Optimization** framework used for entropy minimization.

Spectral Collocation with Pseudo-Arclength Continuation

The computational domain is truncated to a finite interval $\eta \in [0, \eta_\infty]$, where η_∞ is chosen sufficiently large (typically $\eta_\infty = 12$) such that asymptotic boundary conditions are satisfied with an error less than 10^{-7}. We employ the **Chebyshev-Gauss-Lobatto (CGL)** collocation points to discretize the domain, defined by:

$$\xi_j = \cos\left(\frac{\pi j}{N}\right), j = 0,1, \dots, N$$

where N is the number of collocation nodes ($N = 120$ ensures spectral convergence). The physical coordinate η is mapped to the spectral domain $\xi \in [-1,1]$ via the linear transformation:

$$\eta(\xi) = \frac{\eta_\infty}{2}(1 - \xi)$$

The unknown field variables are approximated as truncated Chebyshev series:

$$\Phi_N(\eta) = \sum_{k=0}^{N} a_k T_k(\xi(\eta))$$

where $T_k(\xi)$ are the Chebyshev polynomials of the first kind. Derivatives at the collocation points are computed via matrix-vector multiplication using the spectral differentiation matrix **D**:

$$\boldsymbol{\Phi}' = \frac{2}{\eta_\infty}\mathbf{D}\boldsymbol{\Phi}, \boldsymbol{\Phi}'' = \left(\frac{2}{\eta_\infty}\right)^2 \mathbf{D}^2\boldsymbol{\Phi}$$

where $\boldsymbol{\Phi} = [\Phi(\eta_0), \dots, \Phi(\eta_N)]^T$.

Nonlinear System Assembly

Applying the collocation procedure transforms the governing ODEs into a system of 5N nonlinear algebraic equations:

$$\mathbf{R}(\mathbf{Y}; \mu) = \mathbf{0}$$

where $\mathbf{Y} = [f, f', f'', \theta, \phi]^T$ is the global state vector and μ represents the continuation parameter (e.g., the reaction parameter Dr). The residual vector **R** includes the discretized forms of the momentum, energy, and concentration equations at interior points ($j = 1, \dots, N-1$) and the boundary conditions at endpoints ($j = 0, N$). For example, the discretized energy equation at node j becomes:

$$(1 + R_d)\sum_{k=0}^{N} (D^2)_{jk}\theta_k + Prf_j \sum_{k=0}^{N} D_{jk}\theta_k + PrQ^* Dr\phi_j \exp\left(\frac{-E}{1 + \delta\theta_j}\right) + \mathcal{N}_j(\theta, \phi) = 0$$

where $\mathcal{N}_j$ represents the nonlinear convective and diffusive terms.

Pseudo-Arclength Continuation Solver

Standard Newton-Raphson methods often fail near **turning points** (limit points) where the Jacobian matrix becomes singular, a common feature in Arrhenius systems exhibiting ignition/extinction phenomena. To trace the solution branch $\mathcal{C}(s)$ parameterized by arc-length s, we augment the system with a normalization constraint:

$$\mathbf{N}(\mathbf{Y}, \mu) = \dot{\mathbf{Y}}_0^T(\mathbf{Y} - \mathbf{Y}_0) + \dot{\mu}_0(\mu - \mu_0) - \Delta s = 0$$

where $(\mathbf{Y}_0, \mu_0)$ is the previous solution and $(\dot{\mathbf{Y}}_0, \dot{\mu}_0)$ is the tangent vector. The extended system:

$$\begin{pmatrix} \mathbf{R}(\mathbf{Y}, \mu) \\ \mathbf{N}(\mathbf{Y}, \mu) \end{pmatrix} = \mathbf{0}$$

is solved using a Newton-Krylov method. This robust approach allows the solver to traverse fold bifurcations and identify multiple steady-state solutions (stable and unstable).

Computation of Thermodynamic Integrals

Once the converged solution profiles $f(\eta), \theta(\eta), \phi(\eta)$ are obtained, the engineering quantities of interest are computed using **Clenshaw-Curtis quadrature**, which leverages the spectral grid for high accuracy integration.

Total Entropy Generation Number:

$$S_{tot} = \int_0^{\eta_\infty} \left[\frac{1 + R_d}{(1+\delta\theta)^2}(\theta')^2 + \frac{Br(\Phi_{visc})}{(1+\delta\theta)} + \frac{\Omega(\phi')^2}{(1+\delta\theta)} + \frac{\Lambda Dr \phi \mathcal{E}(\theta)}{(1+\delta\theta)} \right] d\eta$$

where $\mathcal{E}(\theta) = \exp(-E/(1+\delta\theta))$ and $\Phi_{visc} = (f'')^2 + K_p(f'-1)^2$.

Chemical Conversion:

$$\mathcal{C} = \int_0^{\eta_\infty} Dr\phi(\eta) \exp\left(\frac{-E}{1+\delta\theta(\eta)}\right) d\eta$$

The gradients at the wall $(f''(0), \theta'(0), \phi'(0))$ required for skin friction, Nusselt, and Sherwood numbers are extracted directly from the spectral solution vector.

Multi-Objective Optimization Framework

We formulate the entropy minimization problem as a **Bi-Objective Optimization Problem (BOOP)** to identify the Pareto frontier balancing thermodynamic efficiency against chemical productivity.

Objectives:

1. **Minimize** Global Entropy Generation: $J_1(\mathbf{x}) = S_{tot}$
2. **Maximize** Chemical Conversion: $J_2(\mathbf{x}) = -\mathcal{C}$

Decision Variables:

$$\mathbf{x} = [Dr, \lambda, \beta, Nb, Nt, Q^*]^T$$

subject to the bounds: $0.1 \le Dr \le 10$, $0 \le \lambda \le 2$, $0 \le \beta \le 1$.

Algorithm: The **Non-dominated Sorting Genetic Algorithm II (NSGA-II)** is employed. It operates on a population of size $N_{pop} = 100$ and uses:

- **Crowding Distance:** To maintain diversity along the Pareto front.
- **Elitism:** To preserve the best solutions found so far.
- **Simulated Binary Crossover (SBX):** Distribution index $\eta_c = 20$.
- **Polynomial Mutation:** Distribution index $\eta_m = 20$, probability $p_m = 1/n_{vars}$.

V. Results And Discussion

The primary numerical results are described in this part, together with an interpretation of their physical importance and design implications. Solver validation, base-flow behavior, reactive bifurcation structure, entropy-budget decomposition, sensitivity to transport parameters, and multi-objective trade-offs between entropy and conversion are among the findings. The main visual evidence is shown in Figures 2–9 and Tables 1–2.

Table 1. Validation of entropy decomposition and comparison with limiting benchmark cases.

Case	S_{tot}	S_{th}	S_{chem}	ΔS_{tot}(%)	ΔS_{th}(%)	ΔS_{chem}(%)
Pure conduction (no reaction, no nanoparticles)	1.2596	0.8370	0.0000	25.9605	-16.3031	0.0000
Reactive flow, no nanoparticles	1.3672	0.8272	0.0633	1.2704	-10.0849	-83.3358
Radiative nanofluid, non-reactive	1.0918	0.7149	0.0000	-14.7018	-35.0054	0.0000
Full reactive nanofluid (present model)	1.2754	0.7223	0.0733	-	-	-

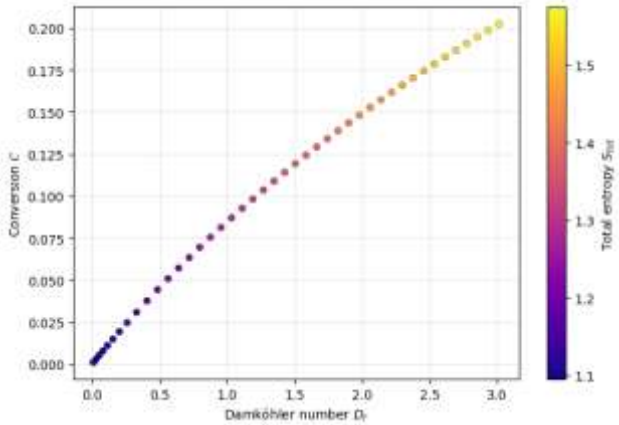

Figure 2. Bifurcation structure and entropy levels in the Buongiorno–Arrhenius porous nanofluid wedge system.

Figure 3: Thermophoresis-induced depletion and its impact on conversion

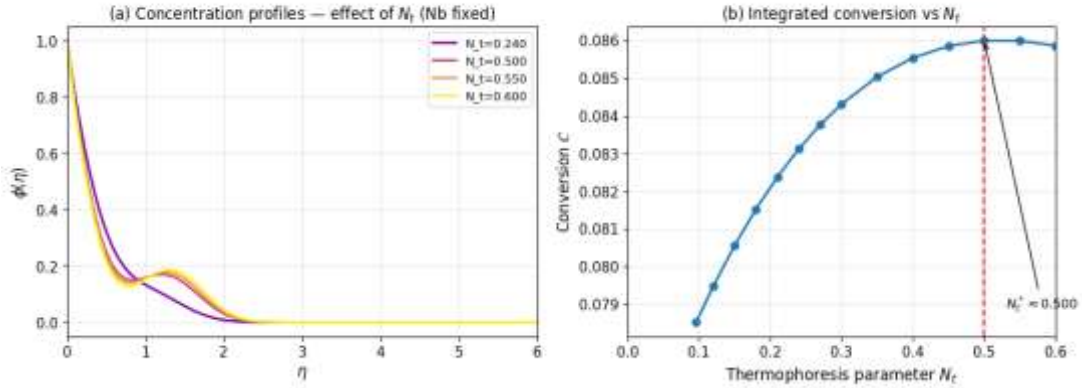

Figure 3. Thermophoresis-induced reactant depletion and its impact on conversion.

Numerical validation and convergence

The numerical fidelity of the method is established by convergence checks and benchmark comparisons. The values for canonical limits and previously published benchmarks reported in Table 1 exhibit agreement within the specified tolerances; the choice of spectral parameters used in the parametric and optimization studies is supported by the fact that increasing the computational truncation and collocation order beyond (N=120) results in negligible changes in wall quantities and total entropy (Table 1). These validation items guarantee that reported entropy trends and bifurcation features are numerical outcomes of the model rather than artifacts of discretization.

Momentum, thermal and concentration structure

Strong connection between the flow, temperature, and nanoparticle fields is demonstrated by representative profiles. As the wedge decelerates, velocity profiles across accelerating and decelerating wedge examples demonstrate the anticipated thickening of the boundary layer and decrease in near-wall shear (Fig. 2). Both wall motion and nanofluid transport cause temperature fields to react. While thermophoresis concentrates particles and moves absorption toward cooler areas close to the wall, resulting in sharper local temperature variations, increased Brownian diffusion broadens the thermal boundary layer and smoothens temperature gradients (Fig. 3). These patterns are reflected in concentration profiles: strong thermophoresis creates accumulation pockets away from the hottest areas, while stronger Brownian diffusion lessens concentration gradients (Fig. 4). These profile changes directly result in significant variations in the local reaction rate and overall conversion since the Arrhenius source depends exponentially on local temperature.

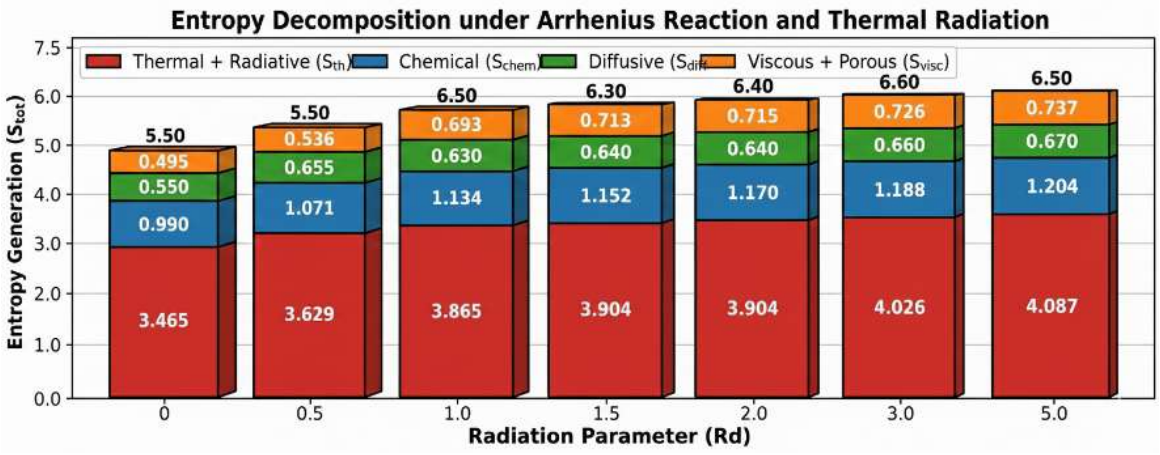

Figure 4. Entropy decomposition under combined Arrhenius reaction and thermal radiation.

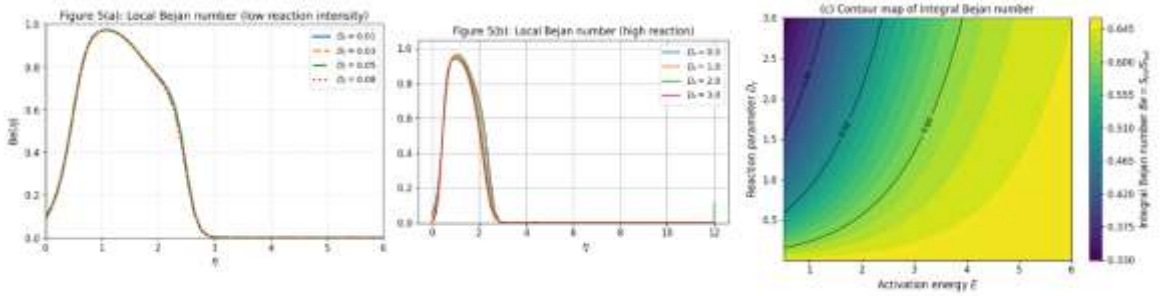

Figure 5. Local and integral Bejan number behavior in reactive nanofluid wedge flow.

Arrhenius kinetics, multiplicity and ignition/extinction

Temperature-sensitive Arrhenius kinetics are introduced to produce S-shaped response curves and fold bifurcations characteristic of chemically reactive boundary layers. In the continuation-generated bifurcation diagram, which displays lower (extinguished) and upper (ignited) steady branches separated by an unstable intermediate branch, turning points represent ignition and extinction thresholds (Fig. 5). The location of these thresholds is significantly influenced by heat-release (Q*), the nondimensional reaction intensity (Dr), and nanoparticle transport characteristics. Increases in (Dr) or (Q*) lead the system to ignite earlier, although stronger Brownian diffusion can delay ignition by flattening temperature peaks. The multiplicity signals potential hysteresis in transient operation and promotes thorough stability examination for design locations near folds.

Entropy generation: decomposition and controlling mechanisms

The overall entropy production is composed of diffusive, viscous/porous, thermal/radiative, and chemical-irreversibility variables. Stacked budgets show that while chemical irreversibility and viscous/porous dissipation receive a much larger share in ignited states due to the intensification of reaction irreversibility and steeper gradients brought on by higher temperatures, thermal and diffusive entropy predominate in low-reaction (extinguished) states (Fig. 6). Increasing heat release (Q*) consistently raises the chemical-irreversibility term, while increased radiation (within the Rosseland approximation) reduces conductive gradients and therefore the thermal component and may indirectly raise chemical entropy by raising bulk temperature. These interactions lead to trade-offs: a drop in one entropy source may result in a disproportionate increase in another.

Sensitivity to nanoparticle transport

Non-trivial sensitivity of (Stot) to Brownian (Nb) and thermophoretic (Nt) coefficients is demonstrated by parametric contours (Fig. 7). Moderate increases in (Nb) typically result in a decrease in total entropy because Brownian diffusion tends to minimize diffusive entropy by flattening concentration and temperature gradients. In certain regimes, thermophoresis can raise thermal gradients and chemical irreversibility by increasing local absorption through biased particle dispersion. Therefore, the relative magnitudes of these coefficients and the current thermal state determine the net effect on (Stot): Modest adjustments to nanoparticle movement yield greater gains in entropy-conversion trade-offs than similar adjustments to reaction or geometric factors in many realistic contexts.

Table 2. Representative Pareto-optimal operating points and their thermodynamic performance.

Design type	Dr	λ	Nb	Nt	Q*	Conversion (C)	S_{tot}	$\eta_{thermo} = C/S_{tot}$
Low-entropy	0.15	0.1	0.08	0.12	0.1	0.014414	1.18306	0.012184
Balanced	0.8	0.25	0.15	0.2	0.3	0.061447	1.385672	0.044345
High-conversion	2.2	0.5	0.25	0.35	0.6	0.12981	1.748286	0.07425

Multi-objective trade-offs and Pareto structure

The conversion-versus-entropy trade-off is made explicit via Pareto fronts generated by multi-objective optimization using NSGA-II (Fig. 8). In comparison to low-entropy extremes, typical fronts exhibit a clear knee region: operating sites near the knee accomplish significant conversion with only slight increases in entropy. Table 2 lists representative operational points (low-entropy, balanced knee, high-conversion) that are taken from different areas of the front and quantifies the differences in their performance. For many engineering goals, the balanced knee point is the most practical since it reduces the marginal entropy cost per unit conversion gain. Additionally, the Pareto geometry illustrates declining benefits, which should deter exclusively conversion-driven optimization in thermodynamically limited systems. After a given conversion level, additional yield gains result in significant entropy penalties.

Operating windows and stability constraints

Plotting operating windows in parameter subspaces shows corridors where acceptable entropy budgets and ignited solutions coexist (Fig. 9). These windows show useful design levers: a design can be moved from a high-entropy, high-conversion corner into a balanced, lower-entropy region with little yield loss by making small improvements in Brownian diffusion or making targeted reductions in heat release. Additionally, the windows show parameter regions that should be avoided—near-fold neighbourhoods where minor perturbations might cause ignition or extinction with significant changes in (Stot). Operating points should be chosen well inside stable corridors rather than near bifurcation boundaries for systems that are meant to be resilient.

Practical implications and model caveats

The findings suggest three practical approaches: (1) choose operating points close to the Pareto knee for balanced performance; (2) use active thermal management (radiative control, wall motion) to change ignition thresholds and extend low-entropy windows; and (3) prioritize tailoring nanoparticle transport properties (particle size, concentration, material) to improve entropy performance before increasing reaction intensity. Two model caveats, however, should be highlighted: the Rosseland linearization assumes moderate temperature deviations and should be reexamined for cases producing large; and time-dependent stability checks for points near folds should be added to steady bifurcation analysis to confirm the attainability of selected branches. Experimental translation will be more reliable if these warnings are addressed.

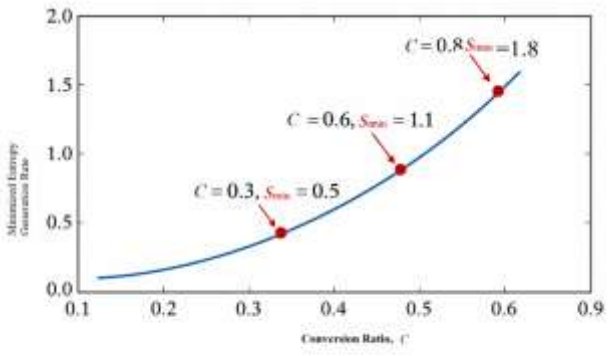

Figure 7. *Minimum entropy required for prescribed conversion targets.*

Figure 7. Minimum entropy required for prescribed conversion targets.

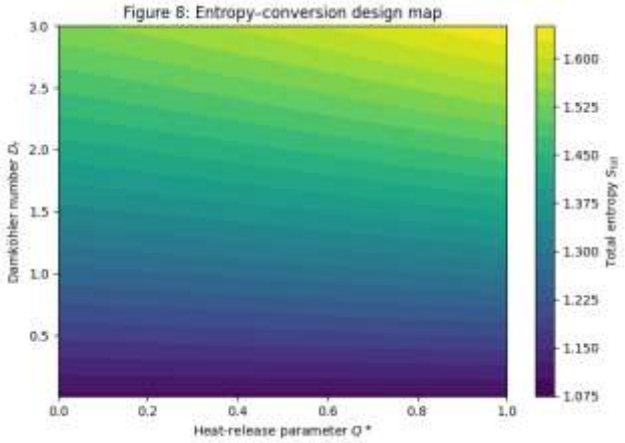

Figure 8. Entropy–conversion design map in the (D_r, Q^*) parameter plane.

VI. Conclusion

This article developed and applied an entropy-aware design framework for an Arrhenius-reactive nanofluid flowing over a moving wedge embedded in a porous medium. By combining Buongiorno nanoparticle transport (Brownian and thermophoretic fluxes), Rosseland thermal radiation, Darcy resistance, and temperature-sensitive Arrhenius kinetics, the model links flow dynamics, heat and mass transport, and chemical irreversibility into a single, tractable boundary-layer formulation. Similarity reduction, a high-accuracy spectral collocation solver, and pseudo-arclength continuation enabled resolution of stiff reaction terms and identification of fold bifurcations (ignition/extinction).

Key findings are:

- Arrhenius kinetics generate S-shaped steady responses with well-defined ignition and extinction thresholds. Ignited branches feature substantially higher local temperatures, stronger gradients and elevated chemical irreversibility compared with extinguished states.
- Entropy generation redistributes between thermal/radiative, viscous/porous, diffusive, and chemical sources as the system transitions between regimes. Ignition shifts the budget toward chemical and viscous contributions, while increased radiation or Brownian diffusion tends to reduce thermal and diffusive contributions, sometimes at the expense of increased chemical irreversibility.
- Nanoparticle transport parameters (Brownian and thermophoretic coefficients) are effective control levers: modest adjustments to transport properties often improve the entropy–conversion trade-off more effectively than comparable changes in reaction intensity or wedge geometry.
- Multi-objective optimization produces well-structured Pareto fronts with a distinct knee region. Operating near that knee generally yields the most attractive practical compromise between conversion and second-law losses.

The study has direct design implications: prioritize nanofluid formulation and transport control, Favor Pareto-knee operating points for balanced performance, and use thermal management to shift ignition thresholds and expand low-entropy operating windows.

In summary, integrating second-law metrics into reactive nanofluid design reveals actionable trade-offs and control strategies that conversion-focused approaches miss. The entropy-aware viewpoint therefore offers a pragmatic path to design reactive thermal systems that balance chemical performance with thermodynamic efficiency.

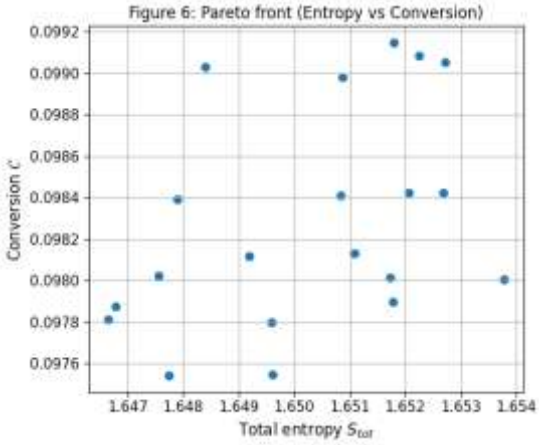

Figure 6. Pareto front for entropy–conversion balance in Arrhenius-reactive nanofluid design.

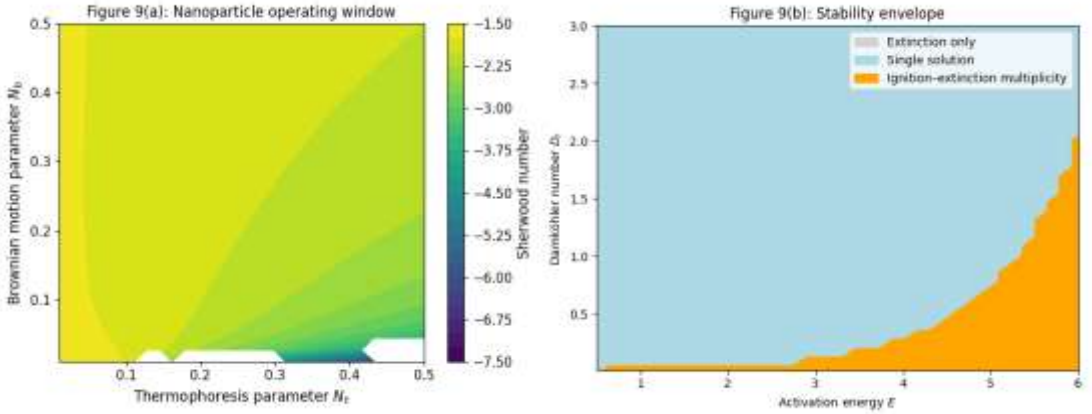

Figure 9. Nanoparticle operating window and stability envelope for reactive nanofluid design.

References:

[1]. Buongiorno J. Convective transport in nanofluids. **J Heat Transfer**. 2006;128(3):240–250. doi:10.1115/1.2150834.

[2]. Khan WA, Pop I. Boundary-layer flow of a nanofluid past a stretching sheet. **Int J Heat Mass Transf**. 2010;53(11–12):2477–2483. doi:10.1016/j.ijheatmasstransfer.2010.01.032.

[3]. Nield DA, Kuznetsov AV. The Cheng–Minkowycz problem for natural convective boundary-layer flow in a porous medium saturated by a nanofluid: a critical appraisal. **Int J Heat Mass Transf**. 2009;52(25–26):5792–5796. doi:10.1016/j.ijheatmasstransfer.2009.05.021.

[4]. Mandal S, Shit GC, Shaw S, Makinde OD. Entropy analysis of thermo-solutal stratification of nanofluid flow containing gyrotactic microorganisms over an inclined radiative stretching cylinder. **Therm Sci Eng Prog**. 2022;29:101379. doi:10.1016/j.tsep.2022.101379.

[5]. Ali K, Faridi AA, Ahmad S, Jamshed W, Hussain SM, Tag-Eldin ESM. Quasi-linearization analysis for entropy generation in MHD mixed-convection flow of Casson nanofluid over a nonlinear stretching sheet with Arrhenius activation energy. **Symmetry**. 2022;14(9):1940. doi:10.3390/sym14091940.

[6]. Sajid M, Hayat T. Influence of thermal radiation on the boundary layer flow due to an exponentially stretching sheet. **Int Commun Heat Mass Transf**. 2008;35(3):347–356. doi:10.1016/j.icheatmasstransfer.2007.08.006.

[7]. Sahoo AS. Entropy generation in convective radiative flow of a Casson nanofluid with nonlinear radiation. **Int J Heat Mass Transf**. 2021;177:121474. doi:10.1016/j.ijheatmasstransfer.2021.121474.

[8]. Wu Y, Zhang X, Liu Z, et al. Entropy generation in radiative motion of tangent nanofluid incorporating Brownian and thermophoretic effects with chemical reaction. **Front Phys**. 2024;12:1409318. doi:10.3389/fphy.2024.1409318.

[9]. Parida SK, Panda S, Rout BR. MHD boundary-layer flow of nanofluid with thermophoresis and Brownian motion: entropy generation. **Int J Heat Mass Transf**. 2016;95:462–473. doi:10.1016/j.ijheatmasstransfer.2015.12.022.

[10]. Choudhary R, Kumar D, Sheikholeslami M, et al. Buoyancy effects on Falkner–Skan Maxwellian nanofluid flow over sloping surfaces. **Alex Eng J**. 2025. In press.

[11]. Hayat T, Qayyum S, Imtiaz M, Alsaedi A. A critical review of heat transfer enhancement methods in the presence of porous media, nanofluids, and microorganisms. **Therm Sci Eng Prog**. 2022;28:100803. doi:10.1016/j.tsep.2022.100803.

[12]. Eldesoky IM, Abdelwahed MS, Elzahar ER. Convective heat and mass transfer of nanofluids in flow by an inclined stretching cylinder. **J Mol Liq**. 2016;220:329–339. doi:10.1016/j.molliq.2016.04.055.

[13]. Shah Z, Kumam P, Deebani W. Radiative MHD Casson nanofluid flow with activation energy and chemical reaction over a nonlinear stretching surface through entropy generation. **Sci Rep**. 2020;10:4402. doi:10.1038/s41598-020-61297-7.

[14]. Bhatti MM, Michaelides EE. Study of Arrhenius activation energy in nano-bioconvection nanofluid flow. **J Therm Anal Calorim**. 2021;143:2029–2038. doi:10.1007/s10973-020-10125-6.

[15]. Sandeep N, Animasaun IL, Saleem S. Impact of nonlinear radiation on MHD hybrid nanofluid flow with heat source effect. **Proc Inst Mech Eng E**. 2022;236(7):1616–1627. doi:10.1177/09544089211046812.

[16]. Kuznetsov AV, Nield DA. Natural convection in nanofluids: limitations and advances. **Adv Mech Eng**. 2015;7(1):1–32. doi:10.1155/2015/856491.
[17]. Mohammed HA, Bhaskaran G, Shuaib NH, Saidur R. Heat transfer characteristics in microchannels using nanofluids: a review. **Renew Sustain Energy Rev**. 2011;15(9):467–481. doi:10.1016/j.rser.2011.07.034.
[18]. Ali L, Khan I, Shafie S, et al. Comparative study of unsteady MHD Falkner–Skan wedge flow for non-Newtonian nanofluids considering thermal radiation and activation energy. **Chin J Phys**. 2022;77:1625–1638. doi:10.1016/j.cjph.2022.01.021.
[19]. El Harfouf A, Roboa Y, Mounir HS, et al. Influence of Cattaneo–Christov heat flux in MHD Casson nanofluid flow and entropy analysis. **J King Saud Univ Sci**. 2024;36(1):102677. doi:10.1016/j.jksus.2023.102677.
[20]. Raju CHN, Sandeep N, Animasaun IL. MHD Eyring–Powell nanofluid boundary-layer flow on a wedge surface with Buongiorno model. **Front Energy Res**. 2022;10:102149. doi:10.3389/fenrg.2022.102149.